The Extraordinary Optical Transmission and Sensing Properties of Ag/Ti Composite Nanohole Arrays

Journal:	*Physical Chemistry Chemical Physics*
Manuscript ID	CP-ART-12-2018-007729.R1
Article Type:	Paper
Date Submitted by the Author:	14-Jan-2019
Complete List of Authors:	Larson , Steven; University of Georgia, Department of Physics and Astronomy Carlson, Daniel; University of Georgia, Physics and Astronomy Ai, Bin; Texas A&M University, Department of Aerospace Engineering Zhao, Yiping; University of Georgia, Department of Physics and Astronomy

The Extraordinary Optical Transmission and Sensing Properties of Ag/Ti Composite Nanohole Arrays

Steven Larson, Daniel Carlson, Bin Ai†, and Yiping Zhao

Department of Physics and Astronomy, University of Georgia, Athens, Georgia 30602

†Corresponding Author. E-mail: binai@tamu.edu

Abstract

Ag/Ti composite nanohole arrays are fabricated by a simple combination of nanosphere lithography, reactive ion etching, and dual e-beam deposition techniques. Based on the measurements of X-ray diffraction, conductivity, and ellipsometry, there exists a Ag composition threshold C_{Ag} = 80 at.% above which Ag is percolated through the entire film. Significant extraordinary optical transmission (EOT) are observed in nanohole samples with composition larger than the threshold. The main EOT peak position, the (1,0) Ag/glass resonance peak, redshifts as the C_{Ag} decreased, but its index sensitivity monotonically increased with C_{Ag} till achieving a value of 300 RIU/nm for C_{Ag} = 100 at.% sample. However, the LSPR peak of the nanoholes can achieve a sensitivity of 390 nm/RIU when C_{Ag} decreases from 100 at.% to 85 at. %. This study demonstrates that besides the shape, size, and measurement configuration, the resonances and sensitivities of nanohole arrays can be effectively predicted and tuned by the composition of a plasmonic composite.

Introduction

Extraordinary optical transmission (EOT) is a surface plasmon resonance (SPR) based effect where more light is transmitted through repeated periodic subwavelength aperture in a metallic film than that can be accounted for by the holes in the film.[1] This property has been widely investigated and applied in the development of optical filters,[2] imaging,[3] photonic circuits,[4] fluorescence,[5] surface enhanced Raman spectroscopy,[6] plasmonic nanochemistry,[7] and sensors.[8] As sensors, nanohole arrays offer both surface plasmon polaritons (SPPs) and localized SPR (LSPR) within their nanohole region, leading to higher sensitivities as compared to plasmonic nanoparticle-based sensors. In addition, some nonconventional fabrication techniques can be used to fabricate nanohole arrays, which are simple, low-cost, and can be easily integrated into microfluidic devices.[9] For a simple hexagonal array of nanoholes, the resonance conditions can be written as,[8, 10]

$$\lambda_{max}(i,j) = \frac{\sqrt{3}}{2}\frac{a_o}{\sqrt{i^2+ij+j^2}}\sqrt{\frac{\varepsilon_m\varepsilon_d}{\varepsilon_m+\varepsilon_d}}, \quad (1)$$

$$\lambda_{min}(i,j) = \frac{\sqrt{3}}{2}\frac{a_o}{\sqrt{i^2+ij+j^2}}\sqrt{\varepsilon_d}\,, \quad (2)$$

where λ_{max} is the EOT resonant wavelength, λ_{min} is the location of the Woods anomaly, a_o is the lattice spacing of the nanohole array, i and j are integer indexes of the peaks, and ε_m and ε_d are the real part of the relative permittivity of the nanohole material and the surrounding environment. These resonance peaks can be quantified for sensing applications by the refractive index sensitivity (RIS) which is defined as the shift of the resonance wavelength ($\Delta\lambda$) with respect to the local index of refraction change (Δn), RIS = $\Delta\lambda/\Delta n$. Clearly, the sensitivity of λ_{max} depends on ε and

$$\frac{d\lambda_{max}}{d\varepsilon_d} = \frac{\sqrt{3}}{2}\frac{a_o}{\sqrt{i^2+ij+j^2}}\sqrt{\left(\frac{\varepsilon_m}{\varepsilon_m+\varepsilon_d}\right)^3}, \quad (3)$$

which represents the sensitivity. Equation (3) shows that the sensitivity depends not only on the a_0 (*i.e.*, the structure of the nanohole array) but also on ε_m. So far, the majority of studies on nanohole EOT properties have focused on tuning the sensing properties by changing the shape or size of the holes[11-13], the lattice spacing of the holes[14], or the measurement configuration of the finalized sensor.[15-17] As shown in Eq.(3), tuning ε_m can also affect the sensitivity. In most up-to-date studies any change in the ε_m is confined to simply changing the material element to another plasmonic active metal, such as Ag[18], Au[11], Pt, Cu[18], *etc*. But recently, studies of composite materials have shown great potential in tuning ε_m, *i.e.*, a simple Maxwell-Garnett effective medium model of the optical constants can be applied to Eq. (3) to show such a change.[10, 19] Several studies have shown that mixtures of two or more noble metals, Ag-Au,[20] Ag-Cu,[21] or Au-Cu[22] can tune ε_m as well as the plasmon resonance to nearly any wavelength between the two LSPR peaks of the individual materials by varying their respective compositions. These mixtures have shown a possibility for improving the sensitivity of LSPR based refractive index sensors. For example, we have shown that the addition of a small composition of MgF_2 (10 at.%) into Ag can significantly improve the sensitivity of the LSPR based sensor from 312 nm/RIU to nearly 696 nm/RIU.[23] Jeong et al. have also shown increased sensitivity by the addition of a small amount of Ti into a nanohelix Ag structure with a RIS reaching 1091 nm/RIU.[24] So far, no systematic studies of composite material systems have been performed for an EOT structure.

Here, we combine nanosphere lithography, reactive ion etching (RIE), and dual-source e-beam deposition to fabricate composite Ag-Ti nanohole arrays with a wide range of Ag compositions. We demonstrate that these nanoholes possess tunable plasmonic properties that

can be easily predicted and controlled. Sensing performances of the different resonance modes are then studied, drawing the conclusion that the SPP peak of the pure Ag nanohole arrays show highest RIS of 300 nm/RIU, while RIS of the LSPR peak can be improved to 390 nm/RIU by a mixed phase of Ag and Ti.

Experimental

Materials

500 nm diameter polystyrene nanospheres (PSNS) (Polyscience, Lot # 679675) were used to form the colloid monolayer onto clean glass slides (Gold Seal, Part# 301) and silicon wafers (University Wafer). Sulfuric acid (Fisher Scientific, 98%), ammonium hydroxide (Fisher Scientific, 98%), and hydrogen peroxide (Fisher Scientific, 30%) were acquired to clean the glass and silicon. Silver and titanium pellets (Plasmaterials, 99.99% and Kurt J. Lesker, 99.995%) were purchased as the evaporation materials. Ethanol (Sigma-Aldrich, 98%), toluene (Fisher Scientific, 99.8%), acetone (Fisher Scientific, 99.8%), and isopropanol (Fisher Scientific, 99.8%) were used for the colloid monolayer preparation and to remove residual PSNS from the substrates after the Ag and Ti deposition. Acetone, 1-hexanol (Tokyo Chemical Industry co., > 98%), chloroform (J.T. Baker, 99%), carbon tetrachloride (Sigma-Aldrich, 99.9%), and toluene were obtained for LSPR sensing measurements. Deionized (DI) water (18 MΩ) was used throughout all the experiments. All chemicals and materials were used without further purification.

Fabrication of the Ag-Ti Composite Nanostructures

Figure 1 summarizes the fabrication steps for making the composite nanohole arrays. First, glass slides and silicon wafers were cut into small pieces with dimensions of 1 cm × 2.5 cm and 1 cm × 1 cm, respectively. Glass substrates were washed in a heated piranha solution, 4:1 volume

ratio of concentrated sulfuric acid to 30% hydrogen peroxide, for 20 min. Silicon substrates were cleaned using the first step of the RCA method, heated in a 5:1:1 ratio of DI water, ammonium hydroxide, and hydrogen peroxide, for 20 min. All substrates were then thoroughly rinsed in DI water; substrates that were not coated with monolayers were then dried under a N_2 gas flow.

Figure 1(a) shows the a_o = 500 nm PSNS monolayers which were prepared using an air-water interface method as previously reported.[22] Briefly, the PSNS suspension was first diluted in DI water to a concentration of 0.01 w/v % and then washed several times *via* centrifugation. Next, the suspension was further diluted with ethanol to a 2:1 volume ratio of PSNS. The resulting suspension was loaded into a syringe and droplets of PSNS suspension were dispensed at a rate of 0.015 mL/min onto the surface of a tilted cleaned glass Petri dish (diameter of 10 cm) containing approximately 24 mL of DI water via a syringe pump. This process continued until a monolayer was formed and covered the entire water surface. A Teflon ring was placed gently on the surface of the water to protect the monolayer film against adhering to the side wall of the glass Petri dish. The water level then was raised. Glass and silicon substrates were carefully slid below the monolayer film. Finally, the monolayer was lowered on the substrates by slowly pumping out the water with a peristaltic pump, followed by drying in the air overnight.

The size of the PSNSs of the monolayer was reduced to d_h = 350 nm by a Trion Technology Phantom III RIE/ICP system (Fig 1(b)). The etching was conducted at 40 mTorr with a 10 sccm oxygen flow, an inductively coupled plasma power of 25 W, and a reactive ion etch power of 10 W for 350 seconds.

The Ag-Ti nanostructures and thin films were fabricated using a custom-built dual source electron deposition system (Pascal Technology) and the deposition configuration is shown in Figure 1(c). The Ag and Ti crucibles were 17.8 cm apart from each other inside the chamber. The

PSNS monolayer coated and uncoated substrates were mounted 53 cm above the crucibles and centered horizontally relative to the two crucibles. With respect to the substrates normal, the vapor incident angle of the Ag and Ti were, θ = -10° and 10°, respectively. After loading the samples, the deposition chamber was pumped down to a base pressure of < 1×10^{-6} Torr. The deposition rate and total thickness of each evaporation source were monitored by two quartz crystal microbalances (QCM) independently, such that the total deposition thickness, *i.e.*, the sum of Ag and Ti thickness, was fixed to be 50 nm, while keeping the total deposition rate R_{Ag} + R_{Ti} = 0.2 nm/s. The relative deposition rates of Ag (R_{Ag}) and Ti (R_{Ti}) were varied to achieve the estimated atomic composition of Ag (C_{Ag}^{Cal}) of 100, 97.5, 95, 92.5, 90, 85, 80, 66, 33, and 0 at.%. During the deposition, the chamber pressure was kept below 1×10^{-5} Torr, and the substrates were rotated azimuthally at a speed of 15 rpm to ensure even mixing of Ag and Ti. After the co-deposition, the substrates were allowed to cool down to room temperature in vacuum before being taken out. Then, as shown in Figure 1(d), the colloid template was removed from the substrate using Scotch tape, and any remaining PSNS residue was removed by rinsing in toluene, acetone, and isopropanol successively.

Optical and Morphological Characterization

The optical transmission spectra of the Ag-Ti nanostructures were measured by an ultraviolet-visible spectrophotometer (UV-Vis, Jasco-750). Atomic force microscopy (AFM) images of the samples were taken with a Park Systems NX-10 AFM. Scanning electron microscopy images and energy dispersive X-ray spectroscopy (EDX) measurements of the nanostructures and thin films were taken by a field emission scanning electron microscope (SEM, FEI Inspect F). The crystal structures of the thin films and nanostructures were characterized by a PANalytical X'Pert PRO MRD X-ray diffractometer (XRD) with a fixed incidence angle of 0.5°. The XRD scans of the thin

films were recorded with a Cu Kα1 radiation (λ = 1.541 Å) in the 2α range from 20° - 80° with a step size of 0.010°. Ellipsometry measurements of the thin films were taken by a spectroscopic ellipsometer (M-2000, J.A Woollam Co., Inc.) at incident angles of 65°, 70°, 75°, and 80°, respectively, over a wavelength range of 370 - 1000 nm. Sheet resistance measurements of the thin film samples were taken by a Keithley 23700 multimeter and a custom four-point probe setup.

LSPR Sensing Measurements

LSPR sensing measurements were performed by immersing nanostructure samples in a quartz cuvette containing either acetone, 1-hexanol, chloroform, carbon tetrachloride, or toluene, then taking the transmission spectra over a wavelength range of 190 nm to 2500 nm. The resultant extinction spectra were then compared to those of the organic solvents, and any intrinsic peaks due to the solvent's absorbance were removed. The LSPR peaks were then fit to determine the peak location and FWHM.

FDTD Calculations

A commercial software package (FDTD Solutions v 8.16.931, Lumerical Solutions Inc.) was used to calculate the transmission spectra and localized electric field distribution of the nanohole arrays. According to the AFM results, the thickness and the hole diameter were set as 50 nm and 300 nm, respectively. A rectangular unit cell consisting of one hole in the center and four quartering holes at the four corners was used with periodic boundary conditions in two dimensions, see Figure S1 of the supplementary information. Perfectly matched layer boundary conditions were used on the top and bottom surfaces of the calculation domain. The auto nonuniform mesh option was selected for the entire simulation domain for higher numerical accuracy. The mesh accuracy was 4. Two monitors of "frequency domain field profile" and "frequency-domain field and power" were set up to calculate the localized electric field distributions and the transmission spectra under

the continuous wave excitation, respectively. The obtained electromagnetic fields were normalized to the magnitude of the incident electric fields. The dielectric constant spectra of the Ag/Ti materials were taken from the ellipsometry measurements.

Results and Discussion

Morphology and Composition Characterization

Figure 2 shows representative AFM images of Ag-Ti nanohole patterns of different Ag compositions (C_{Ag}) where C_{Ag} is the atomic composition of Ag calculated from the deposition rate ratio. As expected, all the samples consisted of regular hexagonal nanohole patterns. The lattice spacing between adjacent hole centers (a_o) was constantly 500 ± 10 nm. The diameter of the nanoholes was 350 ± 10 nm for all of the samples with the largest variation being less than 10 nm. (see supplementary information Table S1) Some polystyrene residue is also detectable in the center of the holes; this residue has been shown in previous studies to have a negligible effect on the optical and sensing properties of the nanohole arrays.[23] The depth of each hole was measured to be h = 50 ± 3 nm. This demonstrates that all of the nanopatterns produced are consistent in shape, size, and thickness, therefore any changes in the optical and sensing properties are purely a function of the composition.

The crystalline properties of the samples were investigated by XRD. The patterns measured are presented in Figure 3(a). The main peaks are marked as cubic Ag (111), (200), (220), and (311). These four peaks are present through 80 at.% Ag, and at lower C_{Ag} only the Ag (111) peak is detectable. No peaks from Ti were observed for any of the samples including the C_{Ag} = 0 at.% sample. The absence of Ti peaks in the XRD patterns is consistent with other studies on e-beam deposited Ti thin films, which showed no distinguishable peaks for thin films less than 100 nm.[25] This is consistent with our conductivity measurements as shown in Fig S2 of the SI, where the

conductivity of the Ag/Ti thin films increases dramatically with C_{Ag} when $C_{Ag} \geq 80$ at.%. Therefore, $C_{Ag} = 80$ at.% Ag is a critical value for Ag to percolate throughout the entire Ag/Ti film. When $C_{Ag} < 80$ at.%. Ag is not percolated and forms small crystals in the composite thin films rather than continuous thin films.

The compositions of the nanostructures were experimentally determined by EDX measurements on the thin film samples deposited on Si substrates. Here, we assume that the compositions of the thin film samples and the nanohole samples are the same because they were prepared simultaneously. Only the composition of the Ag and Ti (C_{Ag}^{M} and C_{Ti}^{M}) were tracked, and the EDX composition was calculated by

$$C_{Ag}^{EDX} = \frac{C_{Ag}^{M}}{C_{Ag}^{M} + C_{Ti}^{M}} . \quad (4)$$

These C_{Ag}^{EDX} were then compared to the C_{Ag}, and the results are plotted in Figure 3(b). A line representing $C_{Ag}^{EDX} = C_{Ag}$ is also drawn for reference. The measured compositions are consistent with those calculated from the deposition rates, with slightly more Ag than expected.

These complex dielectric functions of the composite thin films were measured *via* ellipsometry and are shown in Figure 4. With the decrease of C_{Ag}, the real part ε_1 becomes smaller in the wavelength range of 400 – 550 nm and becomes larger in the wavelength range of 550 – 1000 nm (Figure 4(a)) while the imaginary part ε_2 becomes larger over the entire measured wavelength range (400 nm – 1000 nm). To further quantify the shift in the permittivity the ellipsometry constants were fit to a Drude Lorentz model for the 0 and 100 at.% Ag (i.e., pure Ti and pure Ag films),

$$\varepsilon(\omega) = \varepsilon(\infty) - \frac{\omega_p^2}{\omega^2 + i\omega\Gamma} + \frac{f\omega_l}{(\omega_l)^2 - (\omega)^2 - i\omega\Gamma_l}, \quad (5)$$

where $\varepsilon(\infty)$ is the effective permittivity as the frequency approaches infinity, ω_p is the effective

plasma frequency, and Γ is the effective damping constant. For the pure Ag sample, a Drude term fits both the real and imaginary well, where $\varepsilon^{\mathrm{Ag}}(\infty) = 3.96 + i0.46$, $\omega_p^{Ag} = 8.75$, and $\Gamma^{\mathrm{Ag}} = 0.057$. For the pure Ti sample, one Lorentz term was added, with fitting parameters of $\varepsilon^{\mathrm{Ti}}(\infty) = 25.2 +$ i11.2, $\omega_p^{Ti} = 37.2$, $\Gamma^{\mathrm{Ti}} = 6.43$, $f^{\mathrm{Ti}} = 7.01$, $\omega_l^{Ti} = 2.19$, and $\Gamma_l^{Ti} = 53.3$. All the fitting Ag parameters are consistent with those reported in literature for pure Ag films in the optical region.[26] For the composite samples, a linear combination of the two models was used to fit the dielectric spectra.

$$\varepsilon(\omega) = \alpha_{Ag}\left[\varepsilon^{Ag}(\infty) - \frac{\left(\omega_p^{\mathrm{Ag}}\right)^2}{\omega^2 + i\omega\Gamma^{Ag}}\right] + \alpha_{Ti}\left[\varepsilon^{Ti}(\infty) - \frac{(\omega_p^{\mathrm{Ti}})^2}{\omega^2 + i\omega\Gamma^{Ti}} + \frac{f^{Ti}\omega_l^{Ti}}{\left(\omega_l^{Ti}\right)^2 - (\omega)^2 - i\omega\Gamma_l^{Ti}}\right], \qquad (6)$$

where α_{Ag} and α_{Ti} are fitting constants and all other parameters are fixed based on the results from the 100 at.% and 0 at.% samples. The fitting parameters are shown in Figure S3 of the SI as a function of C_{Ag}. The α_{Ag} initially monotonically decreases as the C_{Ag} decreases until a threshold is met at $C_{\mathrm{Ag}} = 80$ at.%, after which the α_{Ag} decreases dramatically. The α_{Ti} shows the opposite trend. This threshold is also consistent with the value obtained from the crystal size from XRD and the conductivity measurements.

Extraordinary Optical Transmission

Figure 5(a) shows the transmission spectra $T(\lambda)$ of the nanohole arrays with $C_{\mathrm{Ag}} = 100$, 97, 95, 92, 90, and 85 at.% (note that composite nanohole arrays with $C_{\mathrm{Ag}} = 80$, 65, 50, and 33 at. % were also fabricated, but they show weak EOT and thus are not discussed (Figure S4 of the SI)), respectively. All of the spectra show two peaks and two dips, which we denote the peak/dip wavelength as λ_1, λ_2, λ_3, and λ_4, respectively. According to previous reports[27,27-28] and Eqs. (1) and (2), λ_1, λ_2, λ_3, and λ_4 can be assigned as the (1,0) Ag/glass resonance peaks, (1,0) Ag/glass Wood's anomaly transmission minima, an overlap of (1,0) Ag/air and (1,1) Ag/glass resonance peaks, and an overlap of the LSPR peak of the nanoholes[29,30,31] and the (1,0) Ag/air Wood's

anomaly[32] transmission minima, respectively. Also, in Fig. 5(a), the dotted line indicates the ratio of the hole area with respect to the entire area of the film (~ 33%). Such a value means the direct transmission through the nanoholes without considering the effect of SPR and Bethe limit.[33] The transmission intensity exceeds 33% in a wide wavelength range (λ > 700 nm), manifesting the property of EOT. Figure 5(b) shows the corresponding $T(\lambda)$ calculated by FDTD based on AFM images and the ellipsometry measured dielectric functions for different C_{Ag} samples. The overall spectral features are consistent with those obtained experimentally (Fig. 5(a)) but there are some slight differences. There are six spectral features (peaks or dips), which are denoted as λ_1, λ_2, λ_3', λ_3'', λ_4', and λ_4'', respectively, observed in the calculated spectra. The λ_1 and λ_2 are the (1,0) Ag/glass resonance peak and the (1,0) Ag/glass Wood's anomaly transmission minimum, respectively, which corresponds to the λ_1 and λ_2 in Figure 5(a). The λ_3' and λ_3'' are the (1,1) Ag/glass and (1,0) Ag/air resonance peak, respectively. The λ_4' and λ_4'' are the LSPR peak of the nanoholes and the (1,0) Ag/air Wood's anomaly transmission minimum, respectively. Because the real samples are not as perfect as the calculation models, the peaks and dips obtained in the experiments would become broader. Thus, the λ_3' and λ_3'' overlapped, resulting in a broad experimental peak λ_3, and the two weak dips λ_4' and λ_4'' overlapped, resulting in the prominent experimental dip λ_4.

A quantitative comparison of experimental and FDTD results is shown in Figures 5(c) and 5(d). Figure 5(c) plots the location of λ_1 versus C_{Ag}. Also, the corresponding λ_1 of the (1,0) Ag/glass resonance peak calculated based on Eq. (1) and the ellipsometry data are also shown. The overall λ_1-C_{Ag} relationship agrees well for both the experimental and FDTD results, *i.e.*, λ_1 blue shifts with increasing $C_{Ag;}$ but the calculated result based on Eq. (1) shows a much smaller and almost a constant λ_1, which is significantly different from experiment. The plots of the value

of the transmission peak $T(\lambda_1)$ versus C_{Ag} in Fig. 5(d) also show similar trend between the experimental data and the FDTD calculations, *i.e.*, $T(\lambda_1)$ increases with C_{Ag}. However, the $T(\lambda_1)$ value predicted by FDTD is significantly smaller than those experimentally measured for C_{Ag} < 95 at.%. Several reasons may be responsible for the discrepancies. We used the same structural parameters for all the FDTD models, while there may be variations in structure parameters for the samples with different C_{Ag} in the experiments, especially the experiments were measured over a large surface area (the UV-Vis measurement beam spot diameter is ~ 2 mm as compared to hole period 500 nm). In addition, the surface roughness and defects of the experimental samples were not considered in the calculations, which would lead to extra energy loss. As for the λ_2 dip which is the (1,0) Ag/glass Wood's anomaly transmission minimum, it stays almost the same at λ_2 = 665 nm for different C_{Ag} (Figure S5 of the SI), because the Wood's anomaly transmission minima (λ_2) is independent on the metal material according to Eq. (2). However, the λ_4 dip shows a slight blue-shift from 441 to 432 nm when C_{Ag} decreases (Figure S5 of the SI). The λ_4 dip is more complicated than λ_2 peak since it is the overlap of the LSPR of the nanoholes and the (1,0) Ag/air Wood's anomaly transmission minima. The latter would not change with different C_{Ag} according to Eq. (2). The blue-shift was dominated by LSPR of the nanoholes as ε_1 becomes smaller with the decrease of C_{Ag} in the wavelength range λ < 550 nm (Figure 5(a)). In a short summary, the resonance wavelength and intensity of EOT can be tuned by the composition C_{Ag} in Ag/Ti composite materials.

In addition to the locations of the resonance peaks, the local electric field distribution of nanohole array is also very important for different applications. According to previous reports, [34] the nanoholes play a role like a Fabry-Perot resonator, transferring the evanescent wave and radiating the EM wave to the other side. The resonance wavelength and intensity are greatly

influenced by the LSPR of the nanoholes. To better demonstrate the cause of the large red-shift of the λ_1 peak with the decrease of C_{Ag} in experimental data, local electric field distributions of the nanohole arrays with different C_{Ag} were calculated at λ_1 at the metal-glass interface (Figure 6) (and the corresponding top views of the electric field distributions are shown in Figure S6 of the SI). As shown in Figure 6(a), all the samples show highly enhanced electric fields concentrating on the edge of the nanoholes. The field maximum is at the Ag/glass interface, supporting the conclusion that the λ_1 peak is due to the resonance at the Ag/glass interface. Overall, the electric field becomes weaker with the decrease of C_{Ag}. Quantitative plots of the electric field intensity along the white lines (the Ag/glass interface) are shown in Fig. 6(b) and the field maxima *versus* C_{Ag} are shown in Figure 6(c). Clearly, the maximum electric field $|E/E_0|$ decreases from 7 to 3 when C_{Ag} changes from 100 % to 85 %. Such a decrease in the local electric field results in a decrease in the transmission intensity. This decrease in the electric field is also responsible for the larger red-shift of λ_1 obtained experimentally compared to that calculated from Eq. (1). Also one notices that there is a big change in $|E/E_0|^2$ value when C_{Ag} changes from 92.5 at.% to 95 at.%. As shown in Figure 4 and Figure S3, the imaginary part of the dielectric constant ε_2 and linear fitting constants of the combined Drude Lorentz model α also have a sudden change. The ε_2 of C_{Ag} = 95 at.% thin film is very similar to that of C_{Ag} = 100 at.%, while ε_2 of C_{Ag} = 92.5 at.% thin film show a significant difference. Therefore, the nanohole arrays of the C_{Ag} = 95 at.% should show stronger plasmonic effect compared to that of the C_{Ag} = 92.5 at.% sample, i.e., it could exhibit stronger local electric field at the EOT wavelength. From our previous study, there could be a percolation threshold at C_{Ag} = 92.5 at.% above which the property of Ag-Ti thin film changes significantly.[23]

Sensing Performances

The sensing performances of the composite nanohole samples were tested by immersing the samples in a sequence of liquids with increasing *n*. As an example, transmission spectra $T(\lambda)$ of the nanohole arrays with C_{Ag} = 97 % in different liquids are shown in Figure 7(a), the remaining spectra for other samples are presented in Figure S7 of the SI. As shown in Figure 7(a), there are two peaks and two dips in $T(\lambda)$, which correspond to the above assignments of λ_1, λ_2, $\lambda_3^{''}$, and $\lambda_4^{'}$, respectively. In particular, $\lambda_3^{''}$ becomes the (1,0) resonance peak at the Ag/liquid interface as the air was replaced by the liquid. $\lambda_3^{'}$ is not observed in the spectra becasue it shifts to red and thus is obscured by the broad peak λ_1. $\lambda_4^{''}$ becomes undistinguishable with the overlap of $\lambda_4^{'}$. Clealy, the peaks/dip λ_1, $\lambda_3^{''}$, and $\lambda_4^{'}$ show significant red-shifts with the increase of *n*, while λ_2 does not change due to the fact that it is dominated by the surrounding environment of the glass, not the liquids. The RIS of λ_1, $\lambda_3^{''}$, and $\lambda_4^{'}$ is plotted *versus* C_{Ag} as shown in Figure 7(b). For the peak λ_1, the nanohole arrays with C_{Ag} = 100 % shows the highest RIS of 300 nm/RIU, becasue they have the largest local enhanced electric field (Figure 6(a)). RIS of $\lambda_3^{''}$ is nearly a constant at around 160 nm/RIU for all the samples. The electric field at the Ag/liquid interface is relatively weaker than that at the Ag/glass interface becasue of the smaller *n* of the liquid than that of the glass. Thus, the differences of the electric field at $\lambda_3^{''}$ of the samples with different C_{Ag} are relatively smaller than that at λ_1 at the Ag/glass interface, leading to the small RIS and the small variation of RIS of $\lambda_3^{''}$. In additon, RIS of λ_1 is overall larger than the RIS of $\lambda_3^{''}$, which is consistent with previous reports.[8,34-35] For the dip $\lambda_4^{'}$ which is caused by LSPR of the nanoholes, [27,27-28] the RIS becomes higher, from 370 to 390 nm/RIU with the decrease of C_{Ag}. The sensing performence of LSPR of nanohole arrays was rarely studied in previous reports, because its spectral resolution was low compared to that of the EOT peaks.[30] Herein, although the dips $\lambda_4^{'}$ were still weak, their bandwidth was much smaller than that of the EOT peaks. Thus, $\lambda_4^{'}$ was also studied as a

candidate of the tracking features for the plasmonic sensor. The result that RIS of $\lambda_4^{'}$ inceases with more Ti is consistent with the previous report that RIS of LSPR can be improved by the composite material.[23] RIS of LSPR is determined by the dispersion of the real part of the dielectric function of the metal $Re(\varepsilon_m)$ versus the wavelength. The $\frac{dRe(\varepsilon_m)}{d\lambda}\Big|_{\lambda=\lambda_c}$ becomes smaller with the decrease of C_{Ag} and thus the same Δn of the surrounding environment induces a larger change in λ_c, leading to the increased RIS. [23] In addition to the RIS the figure of merit (FOM) was also calculated, where the FOM is defined as the RIS divided by the full width at half maximum of the spectral feature. The FOMs of λ_1, $\lambda_3^{''}$, and $\lambda_4^{'}$ are summarized in Figure 7(c). For all the samples the FOM of λ_1 is below 1 RIU^{-1} and becomes smaller with the decrease of C_{Ag}. FOM of $\lambda_3^{''}$ decreases slightly with respect to C_{Ag} and is in the range of 2 – 3 RIU^{-1}. For $\lambda_4^{'}$, FOM = 12 RIU^{-1} can be obtained for the pure Ag nanohole array. When C_{Ag} becomes smaller, the FOM of $\lambda_4^{'}$ decreases to 2.5 RIU^{-1}. The FOM could be further improved by etching the glass substrate and/or by applying the differential sensing strategies to a linear[8] or circular[24] polarization dependence nanostructure. Overall, the spetctral features show different sensing performances with the change of C_{Ag} based on the different resonance modes.

Conclusion

In a summary, Ag/Ti composite nanohole arrays were fabricated by a simple combination of nanosphere lithography, reactive ion etching, and dual e-beam deposition techniques. AFM was utilized to ensure the shape and size of the nanoholes was consistent across all of the samples. The composition of the samples was controlled by the deposition rate of the individual source during co-deposition and confirmed by EDX and XRD analysis. There was a threshold composition C_{Ag} = 80 at.% above which Ag was percolated throughout the entire thin film, as suggested by the XRD crystal size analysis, conductivity measurements, as well as the dielectric

property obtained from ellipsometry. For samples with C_{Ag} above this threshold, the optical transmission spectra of the nanohole samples showed significant EOT. The main EOT peak, the (1,0) Ag/glass resonance peak, redshifted as the C_{Ag} decreased, but its index sensing RIS monotonically increased with C_{Ag}, *i.e.*, achieving 300 RIU/nm and a FOM of 1 RIU^{-1} for C_{Ag} = 100 at.% sample. However, for a dip induced by LSPR in $T(\lambda)$, the LSPR peak of the nanoholes $\lambda_4^{'}$, the RIS changed from 370 to 390 nm/RIU when C_{Ag} decreased from 100 at.% to 85 at. %, while the FOM was 2.5 RIU^{-1}. Clearly, in this case, the percolation threshold plays an important role to improve the sensor performance. Our study demonstrates that besides the shape, size, and measurement arrangement, the resonances and sensitivities of nanohole arrays can be effectively predicted and tuned by the composition of plasmonic composite materials. Such a tunability can play a very significant role in the future design and application of plasmonic materials.

Associated Content

Supplementary Information: The Supplementary Information is available on the publication website at DOI: XXXXXXXXXX.

FDTD simulation configuration, four-probe conductivity measurements, fitting coefficients based on the Drude-Lorentz model of ellipsometry data, UV-Vis transmission spectra of low C_{Ag} nanohole array samples, additional experimental peak wavelength as a function of C_{Ag}, top-view of the local electric field distributions, and transmission spectra from sensing measurements for samples with different C_{Ag}.

Author Information

Corresponding Author

E-mail: binai@tamu.edu

Department of Aerospace Engineering

Texas A&M University

College Station, Texas 77843

Contributions: The manuscript was written with contributions from all authors. All authors have given their approval to the final version of the manuscript.

Notes: These authors declare no competing financial interests.

Acknowledgments

This work is supported by The National Science Foundation under Grant no. CMMI-1435309 and ECCS-1609815. The authors would also like to thank Dr. Zhengwei Pan for the use of his SEM/EDX.

Figure Captions

Figure 1: A cartoon depicting the fabrication processes: (a) monolayer formation, (b) reactive ion etching, (c) co-deposition, and (d) nanosphere removal.

Figure 2: Representative AFM images of the samples (a_o = 500 nm, d_h = 350 nm) at different Ag composition C_{Ag}.

Figure 3.(a) XRD profiles of the films with different C_{Ag} and (b) the plots of the measured Ag composition C_{Ag}^{EDX} from EDX and Ag crystal size extracted from Scherrer's equation *versus* the predicted C_{Ag}.

Figure 4: The extracted (a) real ε_1 and (b) imaginary ε_2 dielectric spectra from ellipsometry measurements of thin films with different C_{Ag} (solid curves) and fittings (dashed curves) by linear combination of Drude Lorentz models.

Figure 5: (a) The experimentally measured and (b) FDTD calculated transmission spectra $T(\lambda)$ of the Ag/Ti composite nanohole arrays with different C_{Ag}. (c) The plots of the peak location λ_1 obtained experimentally, from FDTD and Eq. (1) *versus* C_{Ag}. (d) The plots of $T(\lambda_1)$ obtained experimentally and from FDTD calculations *versus* C_{Ag}.

Figure 6: (a) Cross section views of local electric field distributions of the Ag/Ti nanohole arrays with different C_{Ag} at λ_1. The plots of (b) $|E/E_0|$ along the while lines in (a) and (c) the maxima $|E/E_0|$ along the white lines *versus* C_{Ag}.

Figure 7: (a) Representative experimental transmission spectra $T(\lambda)$ of the C_{Ag} = 97 at.% Ag/Ti composite nanohole array immersed in different liquids. (b) Plots of RIS of peaks/dip λ_1, $\lambda_3^{''}$, and $\lambda_4^{'}$ *versus* C_{Ag}. (c) The plots of FOM of λ_1, $\lambda_3^{''}$, and $\lambda_4^{'}$ as a function of C_{Ag}.

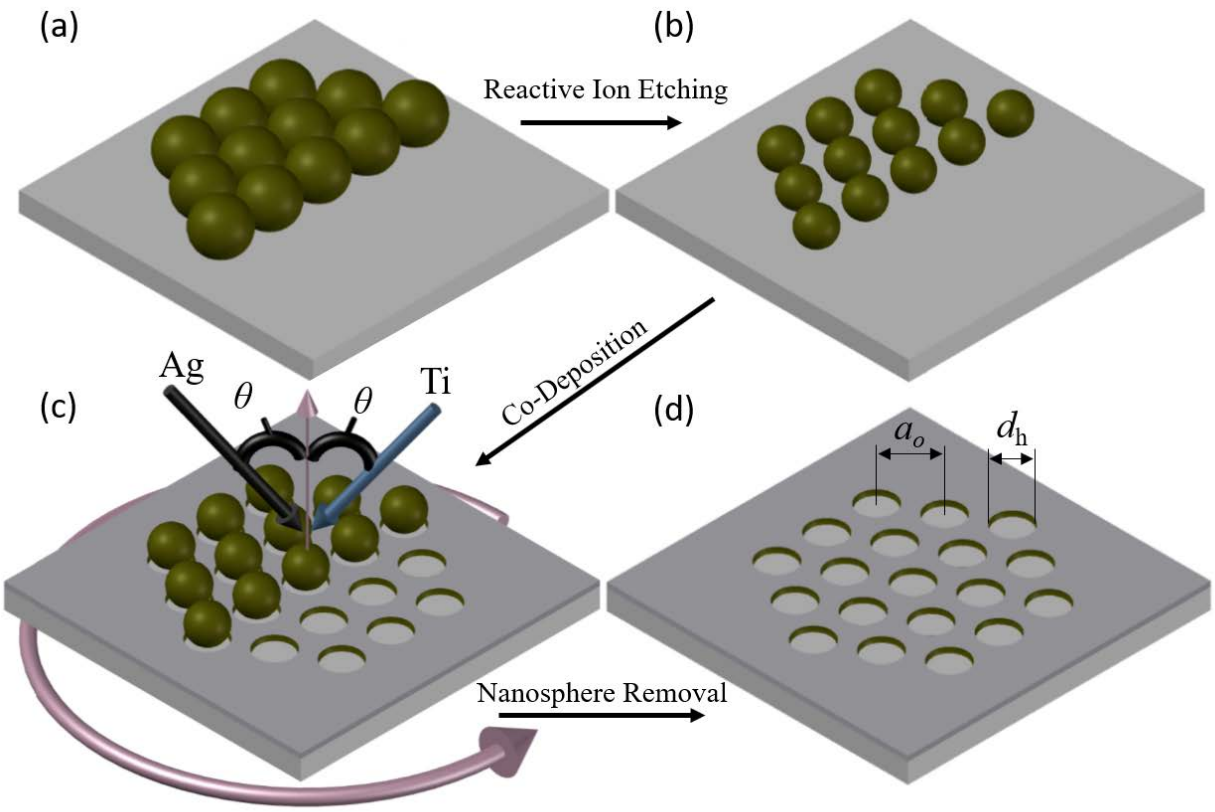
(a)
(b)
Reactive Ion Etching
Ag
θ
θ
Ti
(c)
Co-Deposition
(d)
a_o
d_h
Nanosphere Removal

Figure 1

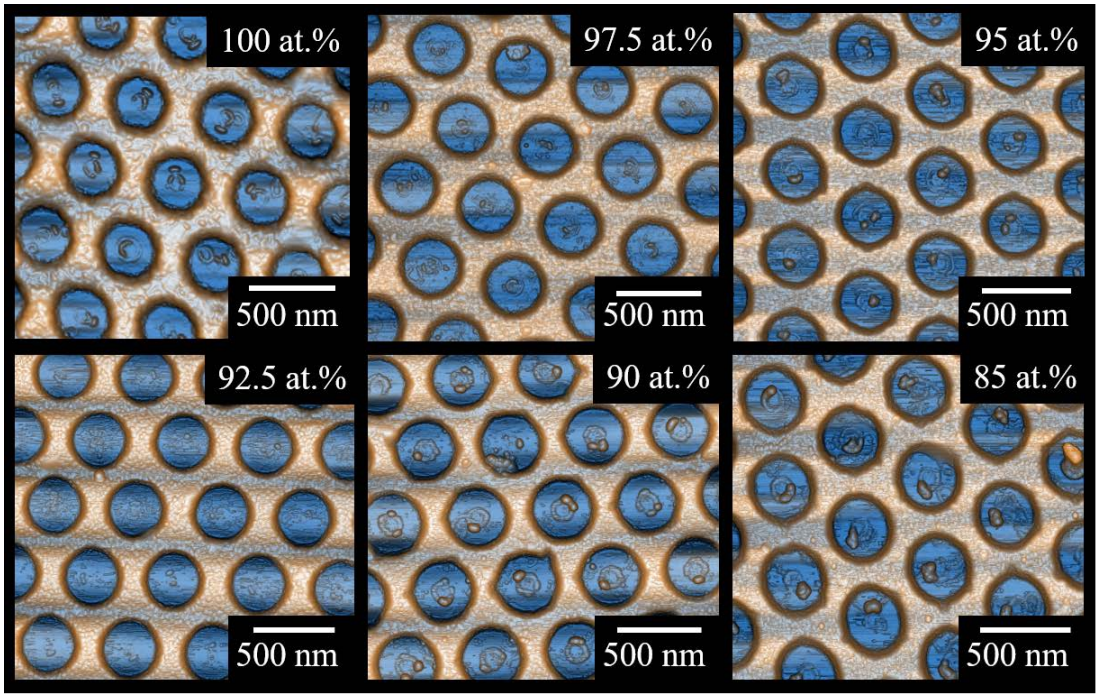
100 at.%
500 nm
97.5 at.%
500 nm
95 at.%
500 nm
92.5 at.%
500 nm
90 at.%
500 nm
85 at.%
500 nm

Figure 2

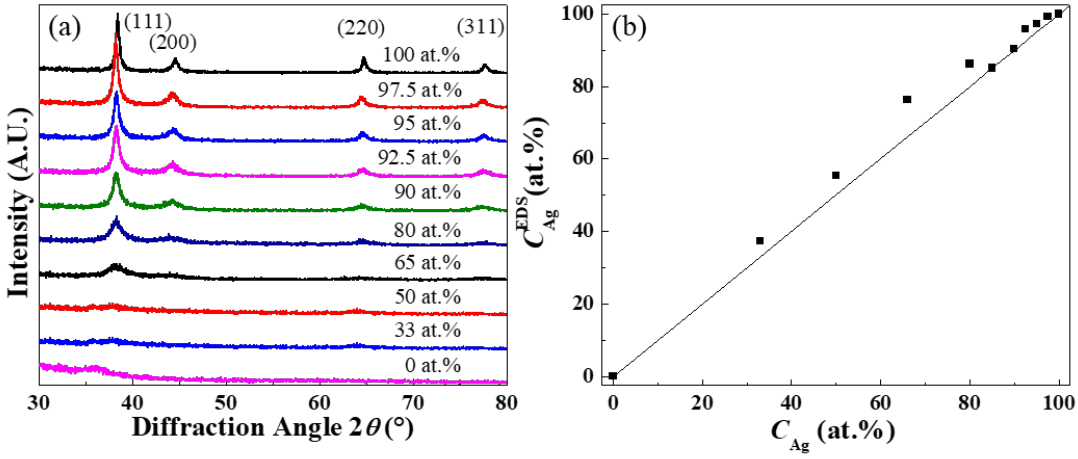
(a)
(111)
(200)
(220)
(311)
100 at.%
97.5 at.%
95 at.%
92.5 at.%
90 at.%
80 at.%
65 at.%
50 at.%
33 at.%
0 at.%
Intensity (A.U.)
Diffraction Angle 2θ(°)
30
40
50
60
70
80
(b)
C_{Ag}^{EDS}(at.%)
C_{Ag} (at.%)
0
20
40
60
80
100

Figure 3

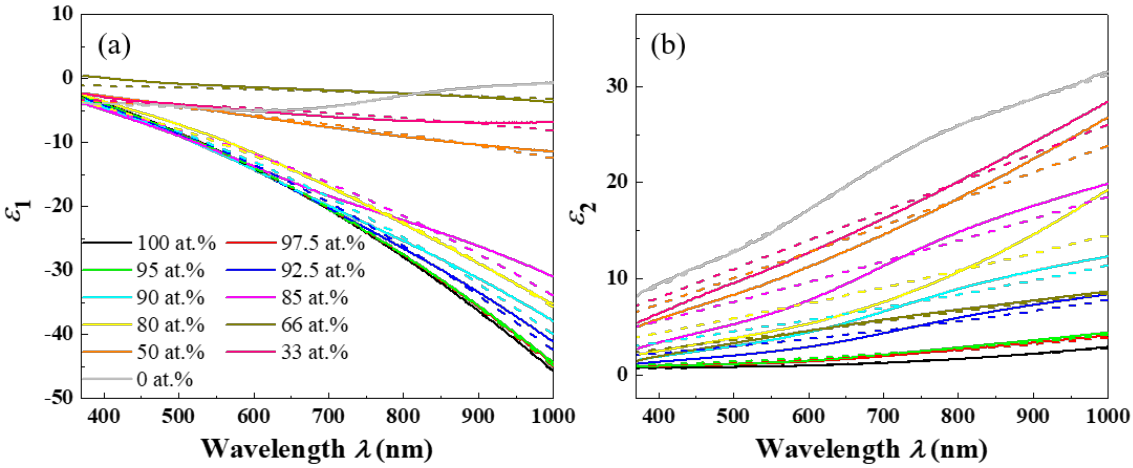
(a)
(b)
ε_1
ε_2
100 at.%
95 at.%
90 at.%
80 at.%
50 at.%
0 at.%
97.5 at.%
92.5 at.%
85 at.%
66 at.%
33 at.%
Wavelength λ (nm)
Wavelength λ (nm)

Figure 4

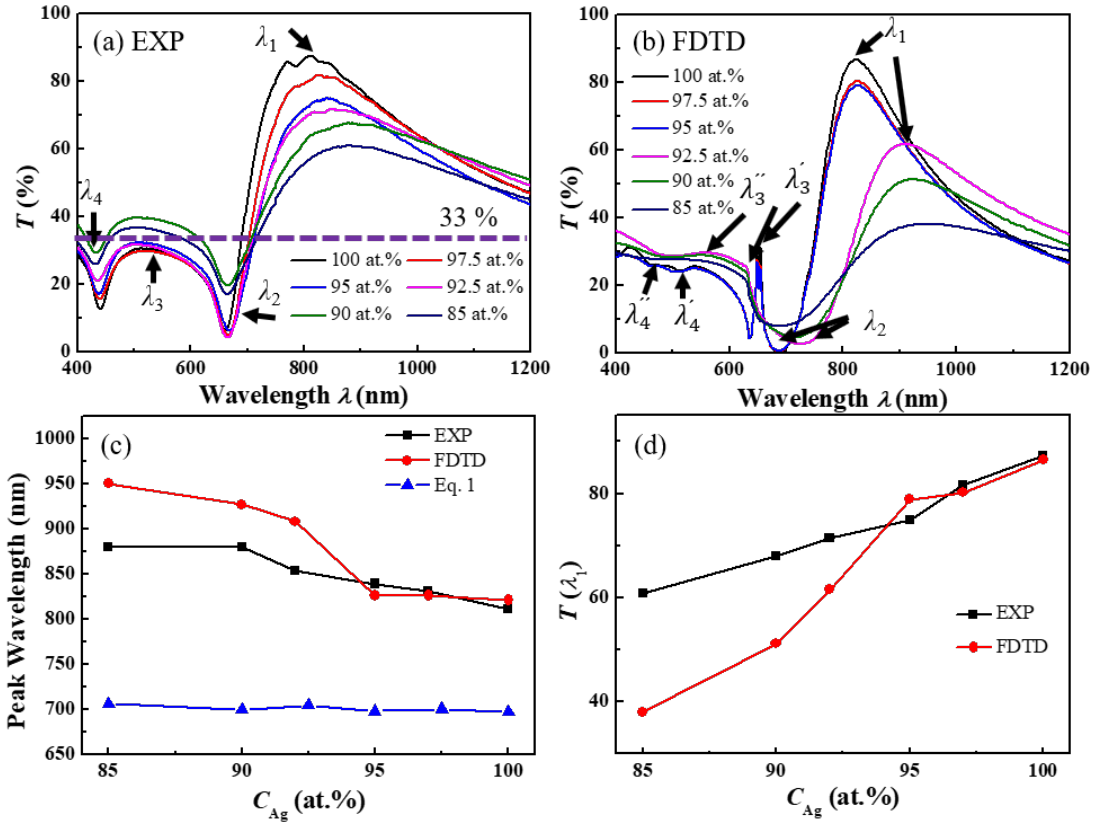
(a) EXP
(b) FDTD
(c)
(d)
T (%)
Wavelength λ (nm)
33 %
100 at.%
97.5 at.%
95 at.%
92.5 at.%
90 at.%
85 at.%
Peak Wavelength (nm)
EXP
FDTD
Eq. 1
T (λ1)
C_Ag (at.%)

Figure 5

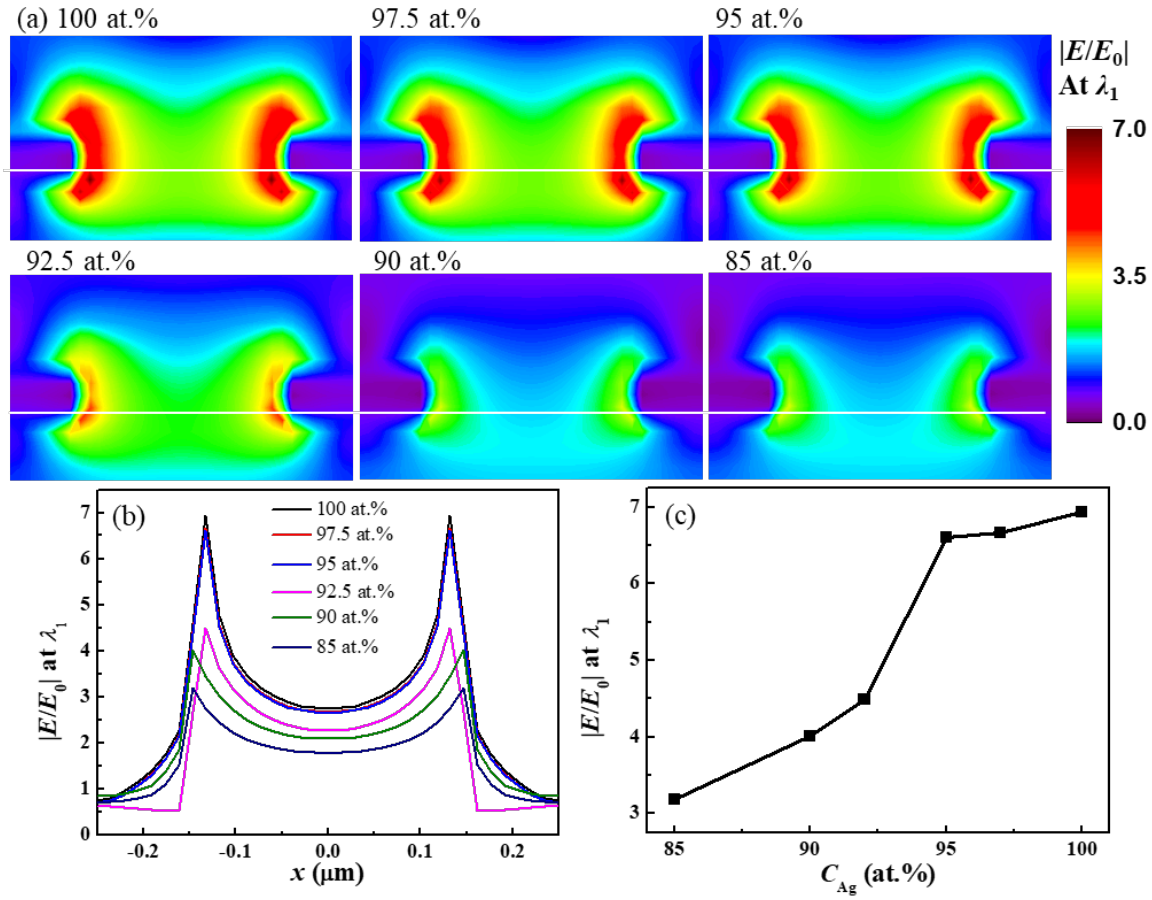
(a) 100 at.%
97.5 at.%
95 at.%
92.5 at.%
90 at.%
85 at.%
|E/E0| At λ1
7.0
3.5
0.0
(b)
100 at.%
97.5 at.%
95 at.%
92.5 at.%
90 at.%
85 at.%
|E/E0| at λ1
x (μm)
(c)
|E/E0| at λ1
C Ag (at.%)

Figure 6

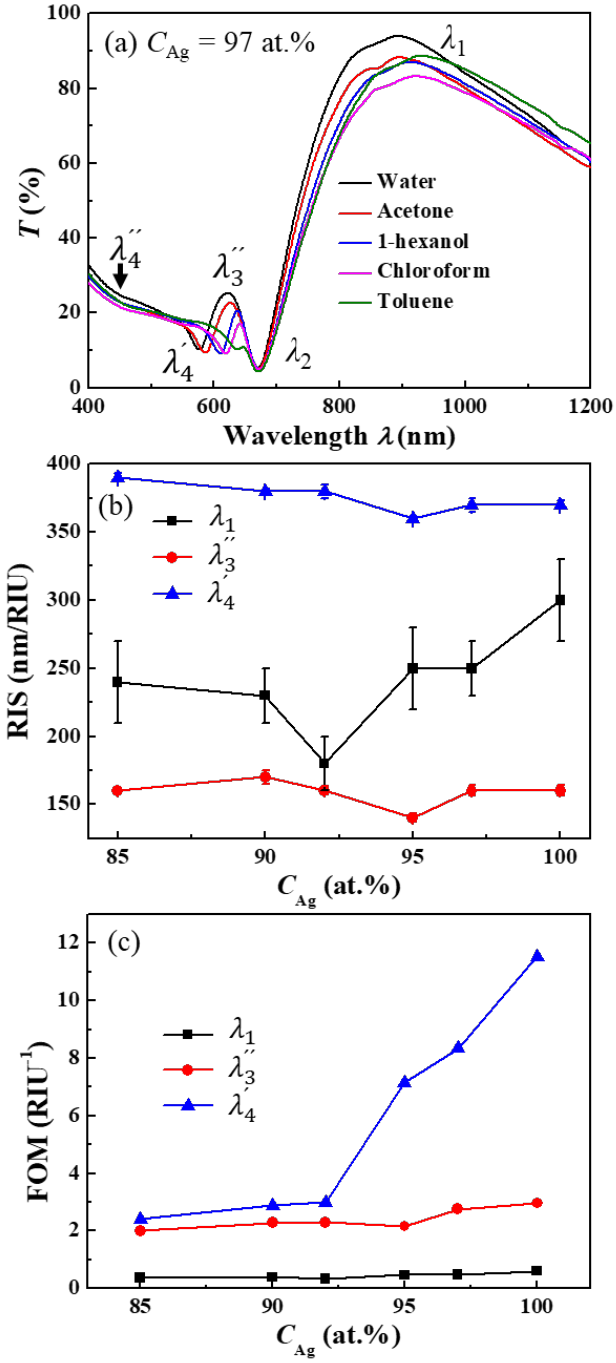
(a) C_{Ag} = 97 at.%
λ_1
λ_2
λ_3''
λ_4''
λ_4'
Water
Acetone
1-hexanol
Chloroform
Toluene
T (%)
Wavelength λ (nm)
(b)
λ_1
λ_3''
λ_4'
RIS (nm/RIU)
C_{Ag} (at.%)
(c)
λ_1
λ_3''
λ_4'
FOM (RIU^{-1})
C_{Ag} (at.%)

Figure 7

References:

1. Grupp, D. E.; Lezec, H. J.; Thio, T.; Ebbesen, T. W. Beyond the Bethe limit: Tunable enhanced light transmission through a single sub-wavelength aperture. *Adv. Mater.* **1999,** *11* (10), 860.
2. DiMaio, J. R.; Ballato, J. Polarization-dependent transmission through subwavelength anisotropic aperture arrays. *Opt. Express* **2006,** *14* (6), 2380-2384.
3. Smolyaninov, II; Elliott, J.; Zayats, A. V.; Davis, C. C. Far-field optical microscopy with a nanometer-scale resolution based on the in-plane image magnification by surface plasmon polaritons. *Phys. Rev. Lett.* **2005,** *94* (5), 057401.
4. Yin, L. L.; Vlasko-Vlasov, V. K.; Pearson, J.; Hiller, J. M.; Hua, J.; Welp, U.; Brown, D. E.; Kimball, C. W. Subwavelength focusing and guiding of surface plasmons. *Nano Lett.* **2005,** *5* (7), 1399-1402.
5. Brolo, A. G.; Kwok, S. C.; Moffitt, M. G.; Gordon, R.; Riordon, J.; Kavanagh, K. L. Enhanced fluorescence from arrays of nanoholes in a gold film. *J. Am. Chem. Soc.* **2005,** *127* (42), 14936-14941.
6. Skehan, C.; Ai, B.; Larson, S.; Stone, K.; Dennis, W.; Zhao, Y. Plasmonic and SERS performances of compound nanohole arrays fabricated by shadow sphere lithography. *Nanotechnology* **2018,** *29* (9), 095301.
7. Ai, B.; Wang, Z.; Moehwald, H.; Zhang, G. Plasmonic nanochemistry based on nanohole array. *Acs Nano* **2017,** *11* (12), 12094-12102.
8. Ai, B.; Basnet, P.; Larson, S.; Ingram, W.; Zhao, Y. Plasmonic sensor with high figure of merit based on differential polarization spectra of elliptical nanohole array. *Nanoscale* **2017,** *9* (38), 14710-14721.
9. Ai, B.; Yu, Y.; Moehwald, H.; Zhang, G.; Yang, B. Plasmonic films based on colloidal lithography. *Advances in Colloid and Interface Science* **2014,** *206*, 5-16.
10. Li, Y., *Plasmonic optics: theory and applications*. SPIE Press: **2017,** 99-129
11. Cheng, K.; Wang, S.; Cui, Z.; Li, Q.; Dai, S.; Du, Z. Large-scale fabrication of plasmonic gold nanohole arrays for refractive index sensing at visible region. *Appl. Phys. Lett.* **2012,** *100* (25), 253101.
12. Ohno, T.; Wadell, C.; Inagaki, S.; Shi, J.; Nakamura, Y.; Matsushita, S.; Sannomiya, T. Hole-size tuning and sensing performance of hexagonal plasmonic nanohole arrays. *Opt. Mat. Express* **2016,** *6* (5), 1594-1603.
13. Molen, K. L. v. d.; Segerink, F. B.; Hulst, N. F. v.; Kuipers, L. Influence of hole size on the extraordinary transmission through subwavelength hole arrays. *Appl. Phys. Lett.* **2004,** *85* (19), 4316-4318.
14. Offermans, P.; Schaafsma, M. C.; Rodriguez, S. R. K.; Zhang, Y.; Crego-Calama, M.; Brongersma, S. H.; Gómez Rivas, J. Universal scaling of the figure of merit of plasmonic sensors. *ACS Nano* **2011,** *5* (6), 5151-5157.
15. Pang, L.; Hwang, G. M.; Slutsky, B.; Fainman, Y. Spectral sensitivity of two-dimensional nanohole array surface plasmon polariton resonance sensor. *Appl. Phys. Lett.* **2007,** *91* (12), 123112.
16. Stark, P. R. H.; Halleck, A. E.; Larson, D. N. Short order nanohole arrays in metals for highly sensitive probing of local indices of refraction as the basis for a highly multiplexed biosensor technology. *Methods* **2005,** *37* (1), 37-47.
17. Rindzevicius, T.; Alaverdyan, Y.; Käll, M.; Murray, W. A.; Barnes, W. L. Long-range

refractive index sensing using plasmonic nanostructures. *J. Phys. Chem. C* **2007,** *111* (32), 11806-11810.
18. Henzie, J.; Lee, M. H.; Odom, T. W. Multiscale patterning of plasmonic metamaterials. *Nat. Nanotechnol.* **2007,** *2*, 549.
19. Aspnes, D. E. Plasmonics and effective-medium theories. *Thin Solid Films* **2011,** *519* (9), 2571-2574.
20. Lee, K. S.; El-Sayed, M. A. Gold and silver nanoparticles in sensing and imaging: Sensitivity of plasmon response to size, shape, and metal composition. *J. Phys. Chem. B* **2006,** *110* (39), 19220-19225.
21. Ingram, W.; Larson, S.; Carlson, D.; Zhao, Y. Ag–Cu mixed phase plasmonic nanostructures fabricated by shadow nanosphere lithography and glancing angle co-deposition. *Nanotechnology* **2017,** *28* (1), 015301.
22. Motl, N. E.; Ewusi-Annan, E.; Sines, I. T.; Jensen, L.; Schaak, R. E. Au−Cu alloy nanoparticles with tunable compositions and plasmonic properties: Experimental determination of composition and correlation with theory. *J. Phys. Chem. C* **2010,** *114* (45), 19263-19269.
23. Larson, S.; Zhao, Y. Localized surface plasmonic resonance and sensing properties of Ag–MgF2 composite nanotriangles. *J. Phys. Chem. C* **2018,** *122* (13), 7374-7381.
24. Jeong, H.-H.; Mark, A. G.; Alarcón-Correa, M.; Kim, I.; Oswald, P.; Lee, T.-C.; Fischer, P. Dispersion and shape engineered plasmonic nanosensors. *Nat. Commun.* **2016,** *7*, 11331.
25. Cai, K.; Müller, M.; Bossert, J.; Rechtenbach, A.; Jandt, K. D. Surface structure and composition of flat titanium thin films as a function of film thickness and evaporation rate. *Appl. Surf. Sci.* **2005,** *250* (1), 252-267.
26. Rioux, D.; Vallieres, S.; Besner, S.; Muñoz, P.; Mazur, E.; Meunier, M. An analytic model for the dielectric function of Au, Ag, and their alloys. *Adv. Opt. Mater.* **2014,** *2* (2), 176-182.
27. Lee, S. H.; Bantz, K. C.; Lindquist, N. C.; Oh, S.-H.; Haynes, C. L. Self-assembled plasmonic nanohole arrays. *Langmuir* **2009,** *25* (23), 13685-13693.
28. Garcia-Vidal, F. J.; Martin-Moreno, L.; Ebbesen, T.; Kuipers, L. Light passing through subwavelength apertures. *Rev. Mod. Phys.* **2010,** *82* (1), 729.
29. Murray, W. A.; Astilean, S.; Barnes, W. L. Transition from localized surface plasmon resonance to extended surface plasmon-polariton as metallic nanoparticles merge to form a periodic hole array. *Phys Rev. B* **2004,** *69* (16), 165407.
30. Degiron, A.; Ebbesen, T. The role of localized surface plasmon modes in the enhanced transmission of periodic subwavelength apertures. *J. Opt. A: Pure Appl. Opt.* **2005,** *7* (2), S90.
31. Chang, S.-H.; Gray, S. K.; Schatz, G. C. Surface plasmon generation and light transmission by isolated nanoholes and arrays of nanoholes in thin metal films. *Opt. Express* **2005,** *13* (8), 3150-3165.
32. Wood, R. W. Anomalous diffraction gratings. *Phys. Rev.* **1935,** *48* (12), 928.
33. Ebbesen, T. W.; Lezec, H. J.; Ghaemi, H.; Thio, T.; Wolff, P. Extraordinary optical transmission through sub-wavelength hole arrays. *Nature* **1998,** *391* (6668), 667.
34. Krishnan, A.; Thio, T.; Kim, T.; Lezec, H.; Ebbesen, T.; Wolff, P.; Pendry, J.; Martin-Moreno, L.; Garcia-Vidal, F. Evanescently coupled resonance in surface plasmon enhanced transmission. *Opt. Commun.* **2001,** *200* (1-6), 1-7.
35. Sannomiya, T.; Scholder, O.; Jefimovs, K.; Hafner, C.; & Dahlin, A. B. Investigation of plasmon resonances in metal films with nanohole arrays for biosensing applications. *Small.*

2011, *7*(12), 1653-1663.